

Contents lists available at ScienceDirect

Ultramicroscopy

journal homepage: www.elsevier.com/locate/ultramic





Wavelength-multiplexed single-shot ptychography

Jonathan Barolak ^{a,*}, David Goldberger ^a, Jeff Squier ^a, Yves Bellouard ^b, Charles Durfee ^a, Daniel Adams ^a

- a Department of Physics, Colorado School of Mines, 1523 Illinois Street, Golden, Colorado 80401, United States of America
- ^b Galatea Laboratory, STI, Ecole Polytechnique Fédérale de Lausanne (EPFL), Neuchâtel, Switzerland

ARTICLE INFO

Keywords: Single-shot ptychography Information multiplexing Coherent diffraction imaging Reference-free Quantitative phase imaging

ABSTRACT

We present the first experimental demonstration of wavelength-multiplexing in single-shot ptychography. Specifically, we experimentally reconstruct the complex transmission profile of a wavelength-independent and wavelength-dependent object simultaneously for 532 nm and 633 nm probing wavelengths. In addition, we discuss the advantages of a more general approach to detector segmentation in single-shot ptychography. A minimization to correct for uncertainties in *a priori* information that is required for single-shot geometries is presented along with a novel probe constraint. Furthermore, this technique is complementary to dual-wavelength interferometry without the need for an external reference. This work is enabling to imaging technologies and applications such as broadband single-shot ptychography, time-resolved imaging by multiplexed ptychography, real-time inspection for laser micro-machining, and plasma imaging.

1. Introduction

Time-resolved amplitude- and phase-contrast imaging methods capable of simultaneously probing with multiple wavelengths are critical in many fields such as ultra-high intensity light-matter interactions, laser material processing, material characterization and plasma imaging. Novel imaging methods capable of investigating harsh environments will provide a better understanding of the underlying physics. As an illustration of where single-shot multiwavelength imaging can provide important information, consider the physics of electrostatic discharge. Many fundamental properties of electrostatic discharges such as plasma channel size, electron and neutral density structure (spatial and temporal), and resistivity are challenging to measure [1]. Common plasma imaging tools such as Schlieren imaging and interferometry are either not quantitative in nature, not directly sensitive to the phase, not spatially (in two dimensions) and temporally resolved, or restricted to weakly scattering plasmas [1-5]. Furthermore, it is important to note that the hydrodynamics of the plasma and neutral atoms can be quite different. For example the plasma created by a laser or electrical discharge can create shock or sound waves that propagate faster than the plasma expansion. Therefore, simultaneous imaging of each structure independently is crucial. By imaging with two wavelengths, typically using dual-wavelength interferometry, the spatial distribution of the electron and neutral background densities may be separated [2].

Multi-wavelength, phase imaging techniques such as Dual-Wavelength Digital Holography (DWDH) are used for material characterization to measure the thickness of a sample in a noncontact, nondestructive manner [6]. In standard digital holography (DH), a sample is probed with a laser beam and the phase is retrieved from the coherent mixing of the probing beam with a reference beam. When the sample is thick and contains large step sizes relative to the wavelength of the probing laser, a 2π -phase ambiguity problem arises preventing it from accurately reconstructing the sample's height profile. By reconstructing the phase from two different wavelength probes, with an appropriate wavelengths ratio, much thicker and rougher samples can be accurately reconstructed. Techniques like dual-wavelength interferometry and DWDH require an external reference with interferometric stability which is experimentally challenging especially when imaging dynamic phenomena such as shock waves generated from plasmas [2,6]. Recent advances in the field of computational imaging offer a promising pathway towards creating a reference-free, time-resolved, amplitude and phase contrast imaging method capable of investigating harsh environments such as electrostatic discharge events, ultra-high intensity light-matter interactions, and material characterization.

Coherent Diffractive Imaging (CDI) is a form of computational imaging that simultaneously retrieves the phase and amplitude of diffracting structures [7–9]. In all CDI methods, coherent radiation probes a sample and diffraction intensities are collected with a pixel-array detector [10–12]. The diffracted intensities along with system

E-mail address: jjbarolak@gmail.com (J. Barolak).

^{*} Corresponding author.

specific constraints provide the necessary requirements for sophisticated phase retrieval algorithms to reconstruct the complex profile of the sample [13]. While many forms of CDI exist, ptychography is a particularly robust implementation that allows simultaneous phase and amplitude contrast imaging of extended objects [14,15].

Ptychography involves probing an object with a finite illumination over many partially overlapped regions of the specimen. Redundancy of information from partially overlapped regions yields a highly constrained phase problem. This redundancy allows ptychographic phase retrieval algorithms to produce reliable, high fidelity, noise-robust reconstructions [16] of both the specimen and the incident illumination. Separating artifacts in the illumination from the object reconstruction represents another advantage when compared to the interferometric techniques previously described. Furthermore, it has been shown that mixed states can be deconvolved, and partial decoherences can be compensated for in advanced reconstruction algorithms, such as ptychographic information multiplexing (PIM) and mixed state decomposition [17,18]. These advanced techniques extended the utility of ptychography to allow for simultaneous imaging with multiple probe illuminations of different wavelengths or polarization states without significant degradation to reconstruction quality as measured by resolution and signal to noise ratio (SNR) [19,20].

While these recent developments in advanced ptychographic phase retrieval algorithms are promising for numerous imaging applications, they require transverse scanning of the object which precludes imaging transient, non-reproducible dynamics. Single-shot ptychography (SSP) overcomes this scanning requirement by breaking up the coherent illumination into smaller beamlets which simultaneously probe the object [21-24]. The SSP setup, shown in Fig. 1 (a) and (b), consists of a 4f imaging system whereby a diffractive optical element (DOE) is imaged to a detector (camera). The DOE, typically an array of pinholes, breaks up the incident beam into smaller beamlets. These beamlets are collimated and overlap at a point referred to as the crossover point. An object is placed some known distance, δ , away from the crossover point. Beamlets diffract off the object and diffraction pattern intensities are collected around each pinhole image. By computationally segmenting the detector, a ptychographic data set is collected in a single-shot. Beamlet locations on the object, analogous to scan positions in scanning ptychography, are calculated using the pinhole image on the detector, the focal length of the second lens, and δ . The diffraction data and calculated probe locations are fed into a conventional scanning ptychographic phase retrieval algorithm, which simultaneously reconstructs quantitative phase and amplitude images of the object and probe [25-27].

Recently, polarization multiplexed single-shot ptychography was experimentally realized [22]. Multiplexing by wavelength, however, has not been experimentally demonstrated in a single-shot ptychographic microscope. Here we present Wavelength-Multiplexed Single-Shot Ptychography (WM-SSP) and provide experimental single-shot, wavelength-multiplexed ptychographic reconstructions. Furthermore, we present improvements to existing single-shot ptychographic methods in the form of a novel probe constraint and a minimization to correct for uncertainty in δ . In addition a discussion of DOE design and detector tessellation is included. WM-SSP represents a critical step towards broadband single-shot ptychography and has applications in a number of other imaging modalities. WM-SSP will offer another channel through which time-slices can be reconstructed in recently developed Time-Resolved Imaging by Multiplexed Ptychography (TIMP). By either setting a time delay to multiple pulses of different probing wavelength or chirping an ultrafast laser pulse, WM-SSP will allow for spatio-temporal characterization of a non-dispersive specimen.

Furthermore, in this article we demonstrate that WM-SSP can also be used for time-resolved birefringence imaging. By orthogonally orienting the polarization states of two different wavelength probes and placing an analyzing polarizer aligned to one probing wavelength's polarization state, WM-SSP can simultaneously image the birefringent and non-birefringent parts of a sample. This will be especially impactful as a real-time feedback diagnostic tool in laser machining where stress-induced birefringence is important.

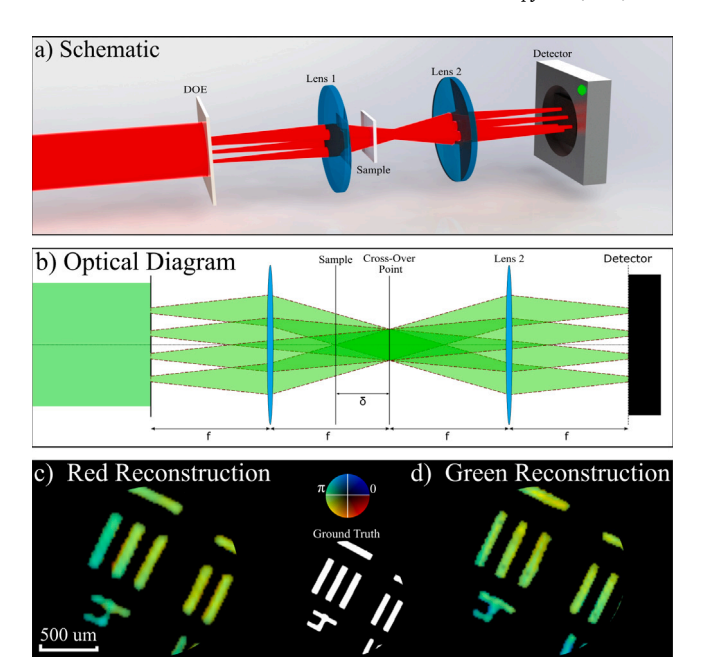


Fig. 1. In (a) a 3D schematic shows the experimental setup with a red illumination. In (b) a detailed diagram of the optical setup is shown. In this optical setup a 4f imaging system is created using two lenses which images the diffractive optical element (DOE) to the detector. The object is placed some distance, δ , away from the crossover point of the beamlets (δ can be varied to the desired level of probe overlap and diffraction pattern diversity). In (c) and (d) complex wavelength-multiplexed reconstructions are shown of an Air-Force Test Pattern. The diffraction data was collected simultaneously from both red and green probing illumination in a single camera exposure. The brightness represents the amplitude and hue represents the phase.

2. Wavelength-multiplexed reconstruction of non-dispersive object

Here we present our first experimental demonstration of ptychographic wavelength multiplexing in a single-shot. The optical setup of our single-shot ptychographic microscope, shown in Fig. 1, consists of a 4f imaging system, a DOE, a sample, and a camera. The 4f imaging system consisted of two 5 cm air-spaced achromatic lenses (Thorlabs part number ACA254-050-A) with high quality AR coatings at the probing wavelengths. The DOE, (a custom made photo-lithography mask: HTA Photomask) has 40 pinholes each with a 55 μ m diameter arranged in a Fermat spiral. The detector (Thorlabs 8051M-USB) was an 8 mega-pixel camera with the wedge and face-plate removed. The camera sensor array has 3296 \times 2472 square pixels with a pixel size, dX of 5.5 μ m. The DOE under-filled the sensor such that the diffraction filled around 50% of the total detector space.

Our first experimental demonstration of WM-SSP used a wavelength-independent object: an Air Force Test Pattern (AFTP). A 532 nm diode-pumped laser and a 633 nm HeNe laser were aligned to be collinear using a dichroic mirror that reflected the 532 nm and transmitted the 633 nm beams. Both laser beams were spatially filtered with a $100 \mu m$ pinhole and collimated with a lens. The beams simultaneously illuminated the WM-SSP optical setup with the AFTP placed a known δ outside of the cross-over point. Diffraction intensities were then collected on the camera using a high dynamic range (HDR) algorithm. The HDR algorithm stitches together images of increasing exposure times to improve the effective bit-depth of the camera. The use of an HDR algorithm could be replaced with a higher dynamic range camera to achieve the similar resolution in a single camera exposure. The reconstructions are shown in (c) and (d) of Fig. 1 with the brightness representing the amplitude and the hue representing the phase. As can be seen in the figure the sample reconstructed with high fidelity for both probing wavelengths as compared to the ground

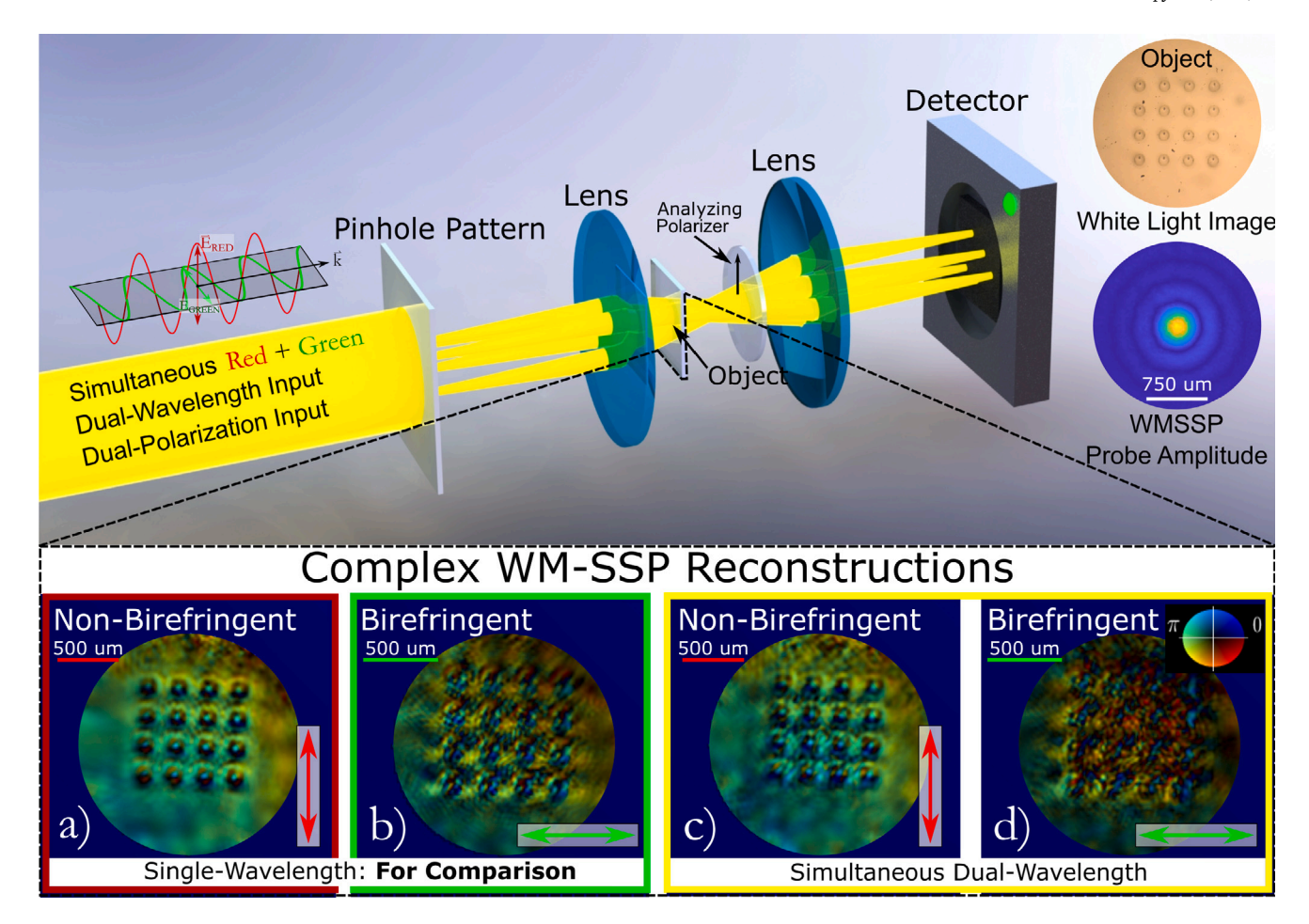


Fig. 2. The WM-SSP setup for imaging the birefringent laser machined sample is pictorially represented. The red probe illumination is vertically polarized and the green probe illumination is horizontally polarized. By aligning an analyzing polarizer after the birefringent object, the red probe images the non-birefringent part of the sample while the green probe images the birefringent part of the sample. The complex object reconstructions from the single-wavelength data are shown in (a) and (b) for comparison against the complex reconstruction from the multi-wavelength data shown in (c) and (d) (intensity represents the amplitude while the color represents the phase). A white light image of the laser-written pattern is shown in the top right of the figure for reference. The amplitude of the probe reconstruction can be found below the white light image. Comparing (c) to (a) and (d) to (b) shows that WM-SSP reproduces high fidelity reconstructions of wavelength-dependent objects. (For interpretation of the references to color in this figure legend, the reader is referred to the web version of this article.)

truth image (shown in the bottom of Fig. 1). Having shown that this works for a nondispersive sample we then moved on to demonstrating this technique on a more complicated specimen.

3. Ptychographic imaging of stress induced birefringence using wavelength multiplexing

To show the utility of WM-SSP, we experimentally reconstructed a wavelength-dependent object. The setup is shown in Fig. 2 and is the same as previously described with the addition of an analyzing polarizer. The wavelength-dependent object was made by exploiting the resulting stress-induced birefringence from femtosecond laser exposure of transparent substrates [28]. The sample imaged is composed of a 4 × 4 grid of cylinders (imaged along the axis so they appear to look like circles) inscribed in a soda-lime substrate using a femtosecond laser. Details about the fabrication methods for these structures can be found in [29,30]. In the case of soda-lime and for the laser exposure conditions used here, the cylinders produce a locally isotropic stress distribution. Specifically, each cylinder has a diameter of 100 µm and consists itself of a stack of 128 laser-written layers. By simultaneously illuminating the sample with a horizontally polarized 532 nm probe and vertically polarized 633 nm probe, the analyzing polarizer separates the birefringent and non-birefringent parts of the objects. Specifically, without the object in the system, the analyzing polarizer was aligned to transmit the 633 nm light while extinguishing the

532 nm light. With the object in the system, any 532 nm light that reaches the detector was rotated by the spatially-dependent, stressinduced birefringence of the object. Thus the reconstructed object for the 532 nm probe represents the birefringent parts of the sample while the 633 nm reconstructed object represents the non-birefringent parts of the sample. Data was taken with both beams simultaneously illuminating the object and each beam individually illuminating the object. We reconstructed the single-wavelength data sets, each running 5000 iterations of a standard ePIE algorithm. These reconstructions serve both as a base to compare the WM-SSP reconstructions against but also as object guesses for the WM-SSP retrieval algorithm. Reconstructions of the dual-wavelength data set ran for 10,000 iterations. The novel probe constraint, discussed in the methods section, and ghost modes (additional wavelength channels where the object is intentionally altered through a translation and/or a rotation) were used in this reconstruction [31]. The reconstructed probe amplitude, complex single-wavelength reconstructions, and multi-wavelength reconstructed objects are shown in Fig. 2. The 633 nm reconstructions (non-birefringent part of the objects) both show a 4×4 array of circles with dots in the middle. The 532 nm reconstructions (birefringent part of the objects) are more complicated but share the same diagonal features going through the 4 × 4 array of laser machined circles (cylinders viewed from the top). The fact that the single-wavelength and multiwavelength reconstructions compare favorably provides confidence that WM-SSP works for wavelength dependent objects. This experiment also provides a novel method for both space and time-resolved quantitative analysis of stress–strain dynamics of laser machining processes. This technique has the capability of providing valuable feedback about the time-dependent stress-induced birefringence created during their machining processes.

4. Methods

There were a number of improvements to the existing SSP methods that we utilized to produce the wavelength-multiplex single-shot reconstructions. In this section we describe the methods we used to create our single-shot ptychography system.

4.1. Diffractive optical element design

To date many SSP setups use a rectangular DOE, one that consists of pinholes arranged in a rectangular grid [21–23]. In SSP, the DOE pattern is analogous to the scanning pattern in standard ptychography. It has been shown that a Fermat spiral scanning pattern in ptychography increases the reconstruction fidelity by preventing regularly repeating artifacts and creating more uniformly overlapped probes on the object [32]. Furthermore, it is known that the Fermat Spiral offers significantly better performance under conditions with imperfections in the data. Data imperfections are unavoidable in SSP from coherent cross-talk between neighboring diffraction patterns, thus using a DOE with pinholes arranged in a Fermat spiral should be more effective than a rectangular grid DOE [33].

For our Fermat spiral DOE we considered three design parameters: pinhole diameter, number of pinholes, and pinhole spacing. Here we considered identical pinholes, although theoretically pinholes size and shape variation could be utilized to optimize systematic performance for specific imaging needs. Pinhole diameter was determined from the oversampling condition, given by $\sigma = \lambda f/(dX_{detector}D)$ where $dX_{detector}$ is the detector pixel size, D is the probe diameter, λ is the probe wavelength, and f is the last lens focal length. For our DOE design, we used a pinhole diameter of 55 μm, which gives an oversampling of 8.2. This calculation is based off the diameter of the airy disk which is defined as the region enclosed by the zeroth-order Jinc function $jinc(x) = J_1(kax/z)/(kax/z)$ with a being the radius of the aperture, k being the angular wavenumber of the incident illumination, z being the distance between the aperture and the observation point, and J_1 being the Bessel function of the first kind of order 1. It is worth noting that illuminating probes generated from a pinhole array type DOE, are strictly not oversampled. This is due to the fact that, at the object plane, the illuminating probes are functionally the full airy pattern and therefore extend to infinity. However, in dimensions higher than one, the oversampling criteria is somewhat relaxed [34]. The number of pinholes determines the theoretical lateral resolution given by

$$dX_{object} = \frac{\lambda f}{dX_{detector} N_{px}} \tag{1}$$

where N_{px} is the number of pixels in the chopped-out diffraction pattern and dX_{object} is the lateral object resolution. Decreasing the number of pinholes increases the chopped-out diffraction pattern size, thus increasing the reconstruction resolution. Therefore, a DOE with only a few pinholes seems favorable, however this must be balanced by the need for redundancy from overlapping probes in a ptychographic data set. Due to these competing effects, we empirically determined that a DOE with 40 pinholes provides a good compromise between resolution and data redundancy for our experimental setup. Finally, pinhole spacing was set such that diffraction signal filled the camera, which minimizes resolution and cross-talk, the coherent superposition of diffraction from adjacent pinholes on the detector. Cross-talk lowers the reconstruction fidelity by introducing mixing of diffraction patterns that is not accounted for in the reconstruction algorithm.

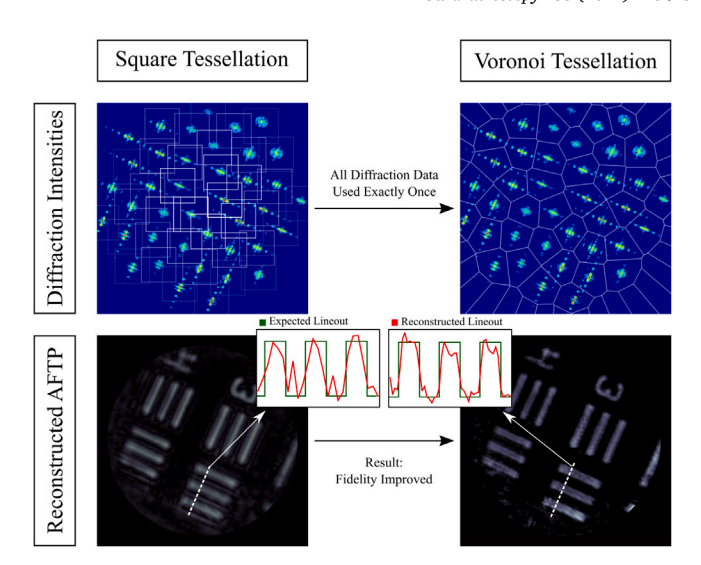


Fig. 3. The images at the top show the square and Voronoi tessellations of diffraction data collected from a SSP system with a Fermat Spiral DOE. Single-wavelength reconstructions were performed from a data set created from both types of tessellation patterns and reconstruction parameters were kept constant for each reconstruction. The amplitude of the reconstructions from the square and Voronoi tessellated Air Force Test Pattern (AFTP) diffraction data are shown. Line-outs from the reconstructions are shown and the expected line-out is plotted on top for comparison. These reconstructions clearly show that the Voronoi tessellation produces higher fidelity images by removing artifacts and flattening the amplitude in the AFTP bars.

4.2. Detector tessellation

We process the data by tessellating the detector and segmenting each beamlet's diffraction pattern. With a rectangular DOE, a square tessellation leads to full use of detector space and no double counting (used in multiple chopped out grids) of diffraction data. Tessellating a Fermat Spiral DOE is more complicated as a square tessellation will lead to unused detector space and/or double counted diffraction data, as illustrated in Fig. 3 . To address this complication, we used a Voronoi tessellation. For a given set of points, p_j , (the centers of each pinhole) the corresponding Voronoi cells are defined as the set of pixels whose distance from a given point in p_j are equal to or less than the distance from any other point in p_j . The Voronoi tessellation leads to full utilization of the detector and gives preferential treatment to diffraction closest to each pinhole, shown in Fig. 3.

To compare square and Voronoi tessellations, an Air Force Test Pattern (AFTP) was imaged at $\delta = 0.9$ cm. Holding everything else constant, the collected diffraction intensities were segmented using both square and Voronoi tessellations. Since the Fermat spiral is not regularly spaced, we chose a square tessellation with cells of 300x300 pixels to balance the effects of double-counting diffraction data and not using enough diffraction data. The Voronoi tessellation will create cells of varying sizes that are chopped out and placed on a square cell of 444 × 444 pixels (padded with zeros). Reconstructions were performed using both tessellations for 1000 iterations, with the same reconstruction parameters. The amplitude of the retrieved images are shown in Fig. 3. The reconstruction from the square tessellation has artifacts, the lines between the real lines of the AFTP, and low fidelity as seen in the non-uniform amplitude distribution within the bars of the AFTP. The Voronoi tessellated reconstruction removes these artifacts and has significantly better fidelity of the flat top AFTP bars. This can be seen more easily in the line-outs shown in Fig. 3.

4.3. δ Correction algorithm

We found that SSP is sensitive to accurate *a priori* knowledge of the distance between the object and the crossover points of the beamlets

(δ as shown in Fig. 1). To show this, we performed a simulated experiment where reconstructions were carried out over a range of δs . The simulated data was collected with a detector made up of 2048 × 2048 square pixels of dX = 10 µm. The 4f imaging system was made up of two 10 cm focal length lenses and the simulated probe wavelength was 532 nm. The simulated DOE consisted of 30 circular pinholes with 50 μm diameters arranged in a Fermat Spiral spaced to fill the detector. The object, the standard camera man image, was placed at a δ of 0.9 cm outside of the crossover point. The field was propagated between lenses using normalized FFTs and between the crossover point and the object plane using the non-paraxial free space transfer function. With the simulated diffraction patterns, reconstructions were performed from 10% below to 10% above the simulated δ . The root mean square (RMS) error was calculated between the reconstructed object at the simulated δ and the reconstructed object at every sampled δ . A plot of the RMS error vs Percent Error in δ is shown in Fig. 4. The graph shows a drastic increase in object RMS error for small errors in δ , which is reflected in the decrease in fidelity of the cameraman shown in the reconstructions at 5% error in δ .

Sophisticated methods must be used in order to accurately measure δ in order to have high reconstruction fidelity. δ can be measured using translation stages oriented axially, however this relies on an accurate knowledge of the crossover point's axial location in free space and the object's axial position. This works for tangible objects, but is not always possible for transient objects. Therefore, we have developed an algorithm that self corrects for inaccurate δ information. Since δ globally scales the beamlets' position on the object, our δ correction algorithm is based on [35]. In our δ correction algorithm, we start by defining the following per iteration error metric:

$$\epsilon = \frac{1}{MNJ} \sum_{f_x, f_y, j} [|\tilde{\psi}_j(f_x, f_y)| - \sqrt{I_j(f_x, f_y)}]^2 \tag{2}$$

where ϵ is the error, M and N are the number of pixels in the X and Y directions respectively, J is the number of beamlets, f_x and f_y are the discrete spatial frequency coordinates in the detector plane, j is the beamlet index, $\tilde{\psi}_j$ is the Fourier transformed exit surface wave of the jth beamlet, and I_j is the measured diffraction pattern intensities from the jth beamlet. Our algorithm solves for δ by finding the gradient of this error metric with respect to α where $\alpha = \frac{\delta}{\ell_f}$, as:

$$\frac{d\epsilon}{d\alpha} = \frac{1}{2MNJ} \sum_{f_x, f_y, j} [1 - \frac{\sqrt{I_j}}{|\tilde{\psi}_j|}] Re(\tilde{\psi}_j^* \frac{d\psi}{d\alpha}) \tag{3}$$

where * represents the conjugate. Here $\frac{d\psi}{da}$ is defined as:

$$\frac{d\psi}{d\alpha} = -2\pi i \mathcal{F}(\mathcal{F}^{-1}(\tilde{P}(f_x, f_y)(f_x X_j + f_y Y_j) \times e^{-2\pi i (f_x X_j + f_y Y_j)})O(x, y))$$

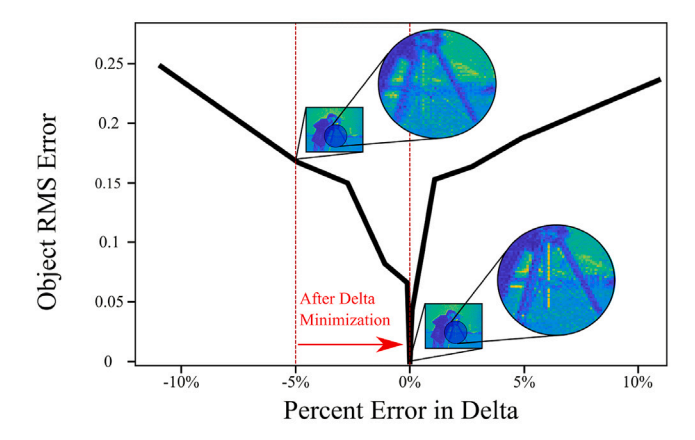
$$(4)$$

where \mathcal{F} and \mathcal{F}^{-1} are the 2D-discrete Fourier transform and inverse Fourier transform operators, respectively, X_j and Y_j are the beamlet positions, x and y are the discrete object space coordinates, \tilde{P} is the Fourier transformed probe, and O is the object. The minimization is then implemented using Newton's method, and after every iteration of the phase retrieval algorithm delta, is updated in the following way:

$$\delta_{n+1} = (\alpha_n + \beta \frac{d\epsilon}{d\alpha})f \tag{5}$$

where β is a step-size parameter that determines how much δ changes in each iteration (for our simulated experiments this beta value was set at 0.4). Use of this algorithm relaxes the required accuracy of the *a priori* δ information. The δ correction algorithm was tested on the simulated data from the previous experiment. Starting with a 5% error in δ , the correction algorithm was able to converge on the correct δ after 55 iterations. A graph showing the percent error in δ as a function of reconstruction iteration is shown in Fig. 4 (b). Our simulation shows that the δ correction algorithm was able to retrieve δ when the guess was within 5% of the actual δ .

a) Object Error as a Function of Error in Delta



b) Reconstruction δ as a Function of Iteration

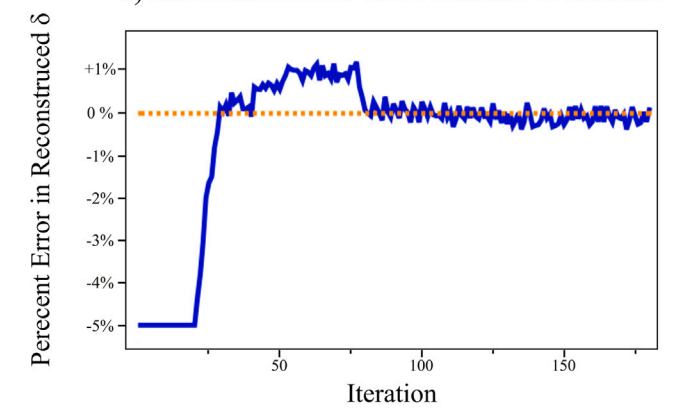


Fig. 4. In (a) a graph of Object RMS Error as a function of the Percent Error in δ is shown. This plot was made using reconstructions over a range of δs from the same simulated data set. The amplitudes from example reconstructions at 5% and 0% error in δ are shown to visibly demonstrate the effect of incorrect knowledge of δ . In (b) a graph of the percent error in reconstructed δ as a function of iteration is shown from a simulated experiment using our δ correction algorithm. The δ correction algorithm started on iteration 25 (with a 5% error in δ) and by iteration 80, it had found the correct δ .

4.4. Multi-wavelength probe constraint

In WM-SSP, SSP is performed simultaneously with probes of multiple wavelengths. Instead of using a single-wavelength phase retrieval algorithm like ePIE, an information multiplexed algorithm, PIM, is used to reconstruct objects for each wavelength [36]. To reinforce WM-SSP, we developed a novel probe constraint specific to the SSP geometry.

In our SSP geometry, pinholes arranged in a Fermat spiral pattern are used to break up the input illumination into multiple beamlets. The pinholes are small relative to the width of the input beam, such that they effectively act as a spatial filter for the beam. Assuming uniform illumination of the DOE, all beamlets for a given wavelength are the same. Probes of different wavelengths, however diffract at different spatial rates. The width of the probe, defined by the zeroth order Jinc, between the first and second lens of the imaging system is given by:

$$W_{probe} = 1.22 \frac{\lambda f}{W_{pinhole}} \tag{6}$$

where W_{probe} is the width of the probe, $W_{pinhole}$ is the width of the pinhole. The pixel size in object space, the basic unit of the detector's pixelated grid propagated to the object, is given by the lateral resolution in Eq. (1). Both the width of the probes and the object

J. Barolak et al. Ultramicroscopy 233 (2022) 113418

space pixel size scale proportional to λ . Therefore, in units of pixels (rather than units of meters), probes of different wavelengths will have exactly the same spatial profile, since the factors of λ cancel. In every iteration of the phase retrieval algorithm, we can enforce this constraint by averaging the updated probes for each wavelength. The relative intensities can still be calculated in each iteration separately, but the spatial profile is constrained to be the same in units of pixels for each wavelength. This probe constraint narrows the solution space that the algorithm has to traverse in order to find the correct object and probe that minimize the error metric in the PIM algorithm.

5. Conclusion

In this paper, we experimentally demonstrated wavelengthmultiplexing in single-shot ptychography. WM-SSP was performed on both an Air Force Test Pattern and a laser-written sample exhibiting stress-induced birefringence. The birefringent nature of the laser-written sample was imaged using orthogonally polarized probes of different wavelength and an analyzing polarizer after the sample. WM-SSP reconstructions were performed to reconstruct the birefringent and non-birefringent parts of the laser-written sample in a single-shot. In addition, improvements to the existing SSP method were proposed and implemented including a discussion of the DOE, detector tessellation method and a minimization to algorithmically correct for uncertainty in the measured δ . A novel probe constraint was introduced based on the geometry of the single-shot setup which constrains the solution space the WM-SSP algorithm has to traverse in order to find the minimum error. WM-SSP represents a major step towards broadband single-shot ptychography and Time-resolved Imaging via Multiplexed Ptychography. Furthermore, as a referencefree wavelength multiplexed phase and amplitude contrast imaging technique, WM-SSP has applications in numerous fields such as plasma imaging, laser machining and the study of high-intensity nonlinear light-matter interactions.

Declaration of competing interest

The authors declare that they have no known competing financial interests or personal relationships that could have appeared to influence the work reported in this paper.

Funding

The authors gratefully acknowledge funding from the National Science Foundation, United States of America under Grant No. 2010359 and Los Alamos National Laboratory, United States of America through contract number 501188.

References

- [1] C. Aragón, J.A. Aguilera, Characterization of laser induced plasmas by optical emission spectroscopy: A review of experiments and methods, Spectrochim. Acta B 63 (9) (2008) 893–916.
- [2] B.V. Weber, S.F. Fulghum, A high sensitivity two-color interferometer for pulsed power plasmas, Rev. Sci. Instrum. 68 (2) (1997) 1227–1232.
- [3] Enrico Traldi, Marco Boselli, Emanuele Simoncelli, Augusto Stancampiano, Matteo Gherardi, Vittorio Colombo, Gary S. Settles, Schlieren imaging: a powerful tool for atmospheric plasma diagnostic, EPJ Tech. Instrum. 5 (1) (2018) 1–23.
- [4] I. Biganzoli, C. Capone, R. Barni, C. Riccardi, Note: Background oriented schlieren as a diagnostics for airflow control by plasma actuators, Rev. Sci. Instrum. 86 (2) (2015) 026103.
- [5] Yoshio Hayasaki, Shin Ichi Fukuda, Satoshi Hasegawa, Saulius Juodkazis, Two-color pump-probe interferometry of ultra-fast light-matter interaction, Sci. Rep. 7 (1) (2017) 1–8.
- [6] Mingguang Shan, Lei Liu, Zhi Zhong, Bin Liu, Yabin Zhang, Direct phase retrieval for simultaneous dual-wavelength off-axis digital holography, Opt. Lasers Eng. 121 (December 2018) (2019) 246–251.
- [7] J.R. Fienup, Reconstruction of an object from the modulus of its Fourier transform, Opt. Lett. 3 (1) (1978) 27–29.

[8] J.R. Fienup, Phase retrieval algorithms: a comparison, Appl. Opt. 21 (15) (1982) 2758.

- [9] Veit Elser, Phase retrieval by iterated projections, J. Opt. Soc. Amer. A 20 (1) (2003) 40.
- [10] Matthew D. Seaberg, Daniel E. Adams, Ethan L. Townsend, Daisy A. Raymondson, William F. Schlotter, Yanwei Liu, Carmen S. Menoni, Lu Rong, Chien-Chun Chen, Jianwei Miao, Henry C. Kapteyn, Margaret M. Murnane, Ultrahigh 22 nm resolution coherent diffractive imaging using a desktop 13 nm high harmonic source, Opt. Express 19 (23) (2011) 22470.
- [11] Christina L. Porter, Michael Tanksalvala, Michael Gerrity, Galen Miley, Xiaoshi Zhang, Charles Bevis, Elisabeth Shanblatt, Robert Karl, Margaret M. Murnane, Daniel E. Adams, Henry C. Kapteyn, General-purpose, wide field-of-view reflection imaging with a tabletop 13 nm light source, Optica 4 (12) (2017) 1552.
- [12] Jlanwei Miao, Pambos Charalambous, Janos Kirz, David Sayre, Extending the methodology of X-ray crystallography to allow imaging of micrometre-sized non-crystalline specimens, Nature 400 (6742) (1999) 342–344.
- [13] Pierre Thibault, Martin Dierolf, Andreas Menzel, Oliver Bunk, Christian David, Franz Pfeiffer, High-resolution scanning X-ray diffraction microscopy, Science 321 (5887) (2008) 379–382.
- [14] J.M. Rodenburg, A.C. Hurst, A.G. Cullis, B.R. Dobson, F. Pfeiffer, O. Bunk, C. David, K. Jefimovs, I. Johnson, Hard-X-ray lensless imaging of extended objects, Phys. Rev. Lett. 98 (3) (2007).
- [15] Pierre Thibault, Martin Dierolf, Oliver Bunk, Andreas Menzel, Franz Pfeiffer, Probe retrieval in ptychographic coherent diffractive imaging, Ultramicroscopy 109 (4) (2009) 338–343.
- [16] Oliver Bunk, Martin Dierolf, Sø ren Kynde, Ian Johnson, Othmar Marti, Franz Pfeiffer, Influence of the overlap parameter on the convergence of the ptychographical iterative engine, Ultramicroscopy 108 (5) (2008) 481–487.
- [17] Darren J. Batey, Daniel Claus, John M. Rodenburg, Information multiplexing in ptychography, Ultramicroscopy 138 (2013) 13–21.
- [18] Pierre Thibault, Andreas Menzel, Reconstructing state mixtures from diffraction measurements, Nature 494 (7435) (2013) 68–71.
- [19] Xukang Wei, Paul Urbach, Ptychography with multiple wavelength illumination, Opt. Express 27 (25) (2019).
- [20] David Goldberger, David Schmidt, Jonathan Barolak, Bojana Ivanic, Charles G. Durfee, Daniel E. Adams, Spatiospectral characterization of ultrafast pulse-beams by multiplexed broadband ptychography, Opt. Express 29 (20) (2021) 32474.
- [21] Pavel Sidorenko, Oren Cohen, Single-shot ptychography, Optica 3 (1) (2016) 9.
- [22] Bing Kuan Chen, Pavel Sidorenko, Oren Lahav, Or Peleg, Oren Cohen, Multiplexed single-shot ptychography, Opt. Lett. 43 (21) (2018) 5379.
- [23] Omri Wengrowicz, Or Peleg, Barry Loevsky, Bing Kuan Chen, Gil Ilan Haham, U. Satya Sainadh, Oren Cohen, Experimental time-resolved imaging by multiplexed ptychography, Opt. Express 27 (17) (2019) 24568.
- [24] Pavel Sidorenko, Oren Lahav, Oren Cohen, Ptychographic ultrahigh-speed imaging, Opt. Express 25 (10) (2017) 10997.
- [25] R.W. Gerchberg, W.O. Saxton, A practical algorithm for the determination of phase from image and diffraction plane pictures, Technical Report 2, 1971, pp. 237–246.
- [26] Pierre Thibault, Martin Dierolf, Oliver Bunk, Andreas Menzel, Franz Pfeiffer, Probe retrieval in ptychographic coherent diffractive imaging, Ultramicroscopy 109 (4) (2009) 338–343.
- [27] Andrew M. Maiden, John M. Rodenburg, An improved ptychographical phase retrieval algorithm for diffractive imaging, Ultramicroscopy 109 (10) (2009) 1256–1262.
- [28] Audrey Champion, Martynas Beresna, Peter Kazansky, Yves Bellouard, Stress distribution around femtosecond laser affected zones: effect of nanogratings orientation, Opt. Express 21 (21) (2013) 24942.
- [29] Ben McMillen, Yves Bellouard, Direct-write diffracting tubular optical components using femtosecond lasers, in: Alexander Heisterkamp, Peter R. Herman, Michel Meunier, Stefan Nolte (Eds.), Frontiers in Ultrafast Optics: Biomedical, Scientific, and Industrial Applications XIV, vol. 8972, SPIE, 2014, 89720Z.
- [30] Ben McMillen, Yves Bellouard, On the anisotropy of stress-distribution induced in glasses and crystals by non-ablative femtosecond laser exposure, Opt. Express 23 (1) (2015) 86.
- [31] Arjun Rana, Jianhua Zhang, Minh Pham, Andrew Yuan, Yuan Hung Lo, Huaidong Jiang, Stanley Osher, Jianwei Miao, Potential of Attosecond Coherent Diffractive Imaging, Technical Report, 2019.
- [32] Xiaojing Huang, Hanfei Yan, Ross Harder, Yeukuang Hwu, Ian K. Robinson, Yong S. Chu, Optimization of overlap uniformness for ptychography, Opt. Express 22 (10) (2014) 12634.
- [33] David Goldberger, Jonathan Barolak, Charles G. Durfee, Daniel E. Adams, Three-dimensional single-shot ptychography, Opt. Express 28 (13) (2020) 18887.
- [34] Robert J. Marks II, Introduction to Shannon Sampling and Interpolation Theory, Springer-Verlag, 1991, pp. 167–225 (Chapter 6).
- [35] Manuel Guizar-Sicairos, James R. Fienup, Phase retrieval with transverse translation diversity: a nonlinear optimization approach, Opt. Express 16 (10) (2008) 7264.
- [36] Darren J. Batey, Daniel Claus, John M. Rodenburg, Information multiplexing in ptychography, Ultramicroscopy 138 (2014) 13–21.